Dynamics of Two-Dimensional Turbulent Bottom Gravity Currents

TAMAY M. ÖZGÖKMEN AND ERIC P. CHASSIGNET

RSMAS/MPO, University of Miami, Miami, Florida

ABSTRACT

In light of previous numerical studies demonstrating a strong sensitivity of the strength of thermohaline circulation to the representation of overflows in ocean general circulation models, the dynamics of bottom gravity currents are investigated using a two-dimensional, nonhydrostatic numerical model. The model explicitly resolves the Kelvin–Helmholtz instability, the main mechanism of mixing in nonrotating bottom gravity currents.

A series of experiments were conducted to explore the impact of density difference and slope angle on the dynamics of bottom gravity currents in a nonrotating and homogeneous environment. The features of the simulated currents; that is, a characteristic head at the leading edge and lumped vortices in the trailing fluid, agree qualitatively well with those observed in laboratory experiments. Quantitative comparisons of speed of descent indicate that laboratory results remain valid at geophysical scales.

Two distinct regimes of entrainment of ambient fluid into bottom gravity currents are identified: (i) the laminar entrainment regime is associated with the initial growth of the characteristic head due to the drag exerted by the fresh fluid in front and (ii) the turbulent entrainment is associated with the Kelvin–Helmholtz instabilities. The turbulent entrainment is found to be much stronger than the laminar entrainment, and entrainment in the turbulent regime is less sensitive to the slope angle than that in the laminar regime. The entrainment is quantified as a function of basic parameters of the system, the buoyancy flux and the slope angle, for the purpose of parameterizing the mixing induced by bottom gravity currents.

1. Introduction

The thermohaline circulation in the ocean is strongly influenced by dense water formation that takes place mainly in high latitude oceans (e.g., Denmark Strait and Faroe Bank Channel: see for a review Dickson et al. 1990; and Borenäs and Lundberg 1988) and in marginal seas (e.g., Mediterranean Sea: Baringer and Price 1997a). Such dense water masses are released into the large-scale circulation in the form of overflows, which are bottom gravity or ''density'' currents. A recent systematic intercomparison between three realistic, eddy-resolving ocean models for the North Atlantic circulation using three different vertical coordinates (depth, isopycnic, or sigma) showed that the modeled large-scale thermohaline circulation was strongly controlled by the details of mixing of the overflows across the Greenland–Scotland region (DYNAMO Group 1997; Willebrand et al. 2001).

Intense evaporation in the Mediterranean Sea produces salty water that flows over the sill in the Strait of Gibraltar (Bryden and Kinder 1991) and forms a bottom density current that descends along the continental slope. If it did not mix with the overlying Atlantic water (Price et al. 1993), the Mediterranean Water would sink to the bottom of the Atlantic Ocean due to its high density. The Mediterranean salinity tongue spreads across the North Atlantic basin at middepths (Lozier et al. 1995). Recent numerical studies (Jia 2000; Özgökmen et al. 2001) indicate that this mixing process may actually play a role in the dynamics of the Azores Current and Countercurrent.

The primary difficulty associated with the representation of bottom density currents in ocean general circulation models (OGCMs) is their small vertical scale, which is typically 100–200 m (Price and Yang 1998). It is also generally accepted from laboratory experiments (Simpson 1969) and observations (e.g., Baringer and Price 1997b) that mixing between density currents and the ambient fluid takes place primarily via the Kelvin–Helmholtz instability. An explicit representation of bottom density currents in numerical models therefore requires not only a small vertical grid scale, but also a horizontal grid scale that is small enough to capture the billows forming near the density interface. Oceanic observations indicate that the typical height-to-length ratio of Kelvin–Helmholtz billows is about 0.1 (e.g., Marmorino 1987). For 10 grid points/billow, the resolution requirements are 10–20 m in the vertical direction and 100–200 m (or approximately $\frac{1}{1000}°$–$\frac{1}{500}°$)

Corresponding author address: Dr. Tamay M. Özgökmen, RSMAS/MPO, University of Miami, 4600 Rickenbacker Causeway, Miami, FL 33149-1098.
E-mail: tamay@rsmas.miami.edu

in the horizontal direction. Such resolution is computationally prohibitive at the present time in ocean general circulation models, implying that parameterizations are needed to represent the mixing of bottom density currents with the ambient water masses.

A prerequisite to the development of such parameterizations is a good understanding of the dynamics of bottom gravity currents. The present level of our understanding is primarily derived from laboratory tank experiments (Ellison and Turner 1959; Simpson 1969; Britter and Linden 1980; Hallworth et al. 1996; Monaghan et al. 1999; Simpson 1982; Turner 1986; Simpson 1987). However, when configured for the small slopes of observed overflows [$O(1°)$], the dense source fluid cannot accelerate within the bounds of typical laboratory tanks [$O(1 \text{ m})$] so that it exhibits a turbulent behavior. For turbulence to occur, laboratory experiments are configured with higher slopes and it is therefore uncertain as to whether the quantitative results derived from laboratory experiments remain valid for geophysical parameters and scales.

The present study therefore has two objectives: (i) to determine whether results based on laboratory experiments of bottom gravity currents remain valid for geophysical scales and parameters and (ii) to gain a detailed understanding of the dynamics of bottom gravity currents and quantify the details of the mixing with the ambient fluid. This paper reports on the use of a nonhydrostatic two-dimensional numerical model to investigate the startup phase of bottom gravity currents in a nonrotating, homogeneous environment. The primary characteristic of these simulations is that the Kelvin–Helmholtz instability, the main mechanism of mixing in bottom gravity currents, is explicitly captured due to the high model horizontal and vertical resolution. The impact of the bottom slope angle and density difference between the gravity current and the environment on the descent speed and the mixing are quantified.

It is found that the simulated bottom gravity currents exhibit similar features to those observed in laboratory experiments, such as a characteristic head at the leading edge and lumped vortices in the trailing fluid. Quantitative comparisons of speed of descent also indicate that the laboratory results remain valid at geophysical scales. The simulated gravity currents exhibit two distinct regimes of entrainment during their descent along the sloping bottom. The first regime of entrainment is associated with the initial growth of the characteristic head due to drag exerted by the fresh fluid in front. Then, there is a sharp transition to a second regime, which is associated with the onset of shear instability in the head and trailing fluid and is characterized by enhanced mixing between gravity currents and ambient fluid. The entrainment in both regimes is quantified and found to be a function of the main parameters of the system, that is, the buoyancy flux at the input location (the strait) and the bottom slope angle.

The paper is organized as follows: In section 2, the method is outlined and the numerical model introduced. The experimental setup and parameters are outlined in section 3. Qualitative and quantitative comparisons of the model results to those from laboratory experiments are presented in section 4. Entrainment characteristics in simulated gravity currents are quantified in section 5. Finally, the principal results are summarized in section 6.

2. Approach

The limitations associated with laboratory experiments in representing oceanic gravity currents raise the question as to whether laboratory results are applicable to oceanic scales and parameters. It is difficult and expensive to set up the geometry of the laboratory tank to represent oceanic scales. It is also difficult to maintain a complex ambient stratification in these tanks. Density currents can be supplied into laboratory tanks by using either a ''constant buoyancy flux'' or a ''constant volume'' approach (e.g., Hallworth et al. 1996). In the latter, a constant volume of dense fluid is released and the volume of the head decreases monotonically with downstream distance, whereas in the former, there is a continual replenishment of the fluid in the head by the constant input of undiluted fluid from the tail. The entrainment characteristics are markedly different between these two cases. Oceanic bottom gravity currents are better represented using the constant-buoyancy flux condition. However, to conduct such constant-buoyancy flux experiments in laboratory tanks with a size $O(1 \text{ m})$, slope angles typically greater than 10° are usually required to accelerate the source fluid and generate a turbulent regime. Continental shelves, on the other hand, have much smaller slopes [$O(1°)$]. Finally, there is the additional difficulty of accurately measuring the mixing between gravity currents and ambient fluid in these laboratory experiments (e.g., Hallworth et al. 1996).

These above limitations can be overcome by using a numerical model. Numerical models, however, introduce other limitations, which are discussed in some detail in the following section.

a. Model philosophy

Bottom density currents have been traditionally investigated using so-called streamtube models. These analytical models have been useful in examining the path and bulk properties of density currents, such as the Mediterranean and Denmark Strait overflows (e.g., Smith 1975; Killworth 1977; Baringer and Price 1997b). Various simplifications are required in these models, such as steady state, motionless ambient fluid and simple topography. In recent years, there have been a number of studies employing more complex models. Jungclaus and Backhaus (1994) used a primitive equation, two-dimensional (x, y) shallow water model with reduced

gravity approximation in the vertical. They conducted idealized experiments to investigate the effects of bottom friction and topography, and also applied their model to the Denmark Strait overflow. Gawarkiewicz and Chapman (1995) used a three-dimensional hydrostatic model to explore the development of a plume with negative buoyancy. They found that the leading edge of the plume forms eddies in the horizontal plane and concluded that instabilities and eddy fluxes are important mechanisms for the transport of dense waters, in contrast to the quasi-steady behavior implied from streamtube models. This conclusion is also supported by numerical studies by Jiang and Garwood (1995, 1996), who used a different three-dimensional, hydrostatic, sigma-coordinate model. Recently, Jiang and Garwood (1998) explored the impact of topographic features, such as cross-slope canyon, cross-slope ridge, and seamount, and also the impact of ambient stratification. They concluded that these factors induce significant changes in the mixing and entrainment between density currents and ambient fluid. Recent observations (Baringer and Price 1997b) of the Mediterranean overflow plume illustrate the importance of the Kelvin–Helmholtz instability in the vertical mixing of bottom gravity currents.

These modeling studies have led to a significant understanding of bottom density currents in the ocean. However, none of the aforementioned studies explicitly resolve the Kelvin–Helmholtz instability, the main mechanism in the vertical mixing and entrainment of density plumes. This is either due to the fact that the chosen model was not able to handle such an instability (e.g., hydrostatic approximation) and/or that the horizontal and vertical grid scale, typically on the O(few kilometers), was not sufficiently small to resolve the instability.

In this paper, we use a two-dimensional (x, z) nonhydrostatic numerical model with high horizontal and vertical resolution. A similar configuration was used by Kao et al. (1978) for laminar surface density currents. The two-dimensional approach is supported by the laboratory experiments of Huppert (1982), Britter and Simpson (1978), Simpson and Britter (1979), and Hacker et al. (1996), which show that the Kelvin–Helmholtz billows in nonrotating laboratory gravity currents have a predominantly two-dimensional structure. In the absence of rotation, the mixing characteristics due to shear instability are similar in two- and three-dimensions (e.g., Lesieur 1997).

b. The numerical model

The governing equations of motion for an incompressible, Boussinesq fluid in two dimensions are nondimensionalized as

$$\psi = \nu_x \psi^*, \qquad (x, z) = h(x^*, z^*), \qquad S = \Delta S S^* \quad (1)$$

where ψ is the streamfunction in the (x, z) plane, ν_x is the horizontal viscosity, h is the thickness of the gravity

current, and ΔS is the salinity difference in the system, equivalent to a density difference $\Delta \rho = \rho_0 \beta \Delta S$. Dropping the asterisk, the model equations become

$$\frac{\partial \zeta}{\partial t} + J(\psi, \zeta) = -\mathrm{Ra}\frac{\partial S}{\partial x} + \frac{\partial^2 \zeta}{\partial x^2} + r\frac{\partial^2 \zeta}{\partial z^2} \quad (2)$$

$$\zeta = \nabla^2 \psi \quad (3)$$

$$\frac{\partial S}{\partial t} + J(\psi, S) = \mathrm{Pr}^{-1}\left(\frac{\partial^2 S}{\partial x^2} + r\frac{\partial^2 S}{\partial z^2}\right) - \kappa(S - S^F), \quad (4)$$

where $\mathrm{Ra} \equiv (gh^3\beta\Delta S)/\nu_x^2$ is the Rayleigh number, the ratio of the strengths of saline-driven convective forcing to viscous drag; $g = 9.81$ m s^{-2} is the gravitational acceleration; $\beta = 7.5 \times 10^{-4}$ psu^{-1} is the salinity contraction coefficient for seawater in the linear equation of state $\rho = \rho_0[1 + \beta\Delta S]$; $r \equiv \nu_z/\nu_x = K_z/K_x$ is the ratio of vertical to horizontal diffusivities; $\mathrm{Pr} \equiv \nu_x/K_x$ is the Prandtl number; and $\kappa \equiv kh^2/\nu_x$ with k being the relaxation frequency for salinity and S^F is the forced salinity value of the bottom density current. Here

$$J(a, b) = \frac{\partial a}{\partial x}\frac{\partial b}{\partial z} - \frac{\partial b}{\partial x}\frac{\partial a}{\partial z}$$

is the Jacobian and

$$\nabla^2 = \frac{\partial^2}{\partial x^2} + \frac{\partial^2}{\partial z^2}$$

is the Laplacian.

The prognostic equations (2) and (4) are advanced in time using a predictor–corrector type leapfrog method (Gazdag 1976). The Jacobian operator is computed using the formulation proposed by Arakawa (1966) that conserves kinetic energy and enstrophy, while accurately maintaining the property $J(a, b) = -J(b, a)$. All other differential operators are approximated by central differences. The diagnostic equation (3) is inverted using a fast Fourier transform solver (Swarztrauber 1977).

The numerical model is based on code previously employed in microscale double-diffusive convection studies (Özgökmen et al. 1998; Özgökmen and Esenkov 1998). The numerics of the code have been extensively tested for conservation properties, and the general numerical implementation has been also used in previous modeling studies (Özgökmen et al. 1997; Özgökmen and Chassignet 1998; Özgökmen et al. 2001). The computational efficiency is increased by recognizing that the downstream evolution of bottom gravity currents resembles that of a shock wave; that is, perturbations are not felt downstream of the head. By tracking the position of the head of the density current and its area of influence, and by constraining the calculations to that portion of the domain, substantial computational gain is obtained during the initial phase of the integrations.

TABLE 1. Parameters of the numerical experiments.

Basin size (x, z)	20 km × 1 km
Bottom slope angle	$1° \leq \theta \leq 5°$, see Table 2
Salinity difference	0.5 psu $\leq \Delta S \leq$ 3 psu, see Table 2
Viscosity (x, z)	$\nu_x = 7$ m² s⁻¹, $\nu_z = 7 \times 10^{-5}$ m² s⁻¹
Diffusivity (x, z)	$K_x = 1$ m² s⁻¹, $K_z = 1 \times 10^{-5}$ m² s⁻¹
Input relaxation coefficient	$\kappa = 21\ 600^{-1}$ s⁻¹
Resolution (x, z)	$\Delta x = \Delta z = 5$ m
Time step	Varies with CFL criterion, typically $O(0.1$ s)
Rayleigh number	$253 \leq$ Ra ≤ 1520
Prandtl number	Pr = 7
Diffusivity ratio	$r = 10^{-5}$

3. Experimental setup and parameters

The majority of the published theoretical and laboratory studies has focused on two controlling factors: the density difference between the gravity current and the ambient fluid and the bottom slope angle. Results from nine numerical experiments with geophysical scales and parameters are presented: three slope angles, $\theta = 1°$, 2.5°, and 5°, on the order of continental slope values, and three densities controlled by the salinity difference from the ambient fluid, $\Delta S = 0.5$, 1.5, and 3.0 psu, in the density range of oceanic overflows (Price and Baringer 1994). These experiments are conducted in the absence of ambient stratification and the system is driven purely by the excess salinity (density) of the gravity current.

The parameters and characteristics of these experiments are tabulated in Tables 1 and 2. The domain is 20 km wide and 1 km deep, discretized by a grid of 4001 × 201 points (or a constant grid spacing of 5 m). This grid spacing is small enough not only to resolve the Kelvin–Helmholtz billows (the scales of which were discussed earlier), but to also make the mixing induced by the step topography negligible. The horizontal resolution is "slope resolving" since it satisfies the criterion $\Delta x < \Delta z \tan\theta$ (Winton et al. 1998). For the maximum slope angle of $\theta = 5°$, the criterion gives $\Delta x < 57$ m, which is clearly satisfied by the 5-m horizontal grid scale used in this study. In addition, the volume/depth of light fluid at the corner of each topographic step must be much less than the volume/depth of the descending dense gravity current. In our simulations, the ratio of the area of "step water" to the area of the overlying bottom density current is typically $O(10^{-2})$. In terms of convergence, the results remain the same with a grid spacing of 10 m. Significant differences become apparent with a grid spacing of 50 m.

Since one of the objectives of the paper is to determine whether results based on laboratory experiments remain valid for geophysical scales, we neglect rotation since the great majority of laboratory experiments were conducted in the absence of rotation. The scale at which the Coriolis force becomes comparable to buoyancy force is a complex function of the slope angle, stratification, and friction (e.g., Griffiths 1986). A simple scaling is given by the radius of deformation $\sqrt{g'h}/f$, which varies at midlatitudes between 8 km (for $\Delta S = 0.5$ psu) and 20 km (for $\Delta S = 3.0$ psu). Rotation is therefore not important at the scale at which the experiments are conducted in this study.

The ratio of the vertical and horizontal diffusivities is set to $r = 10^{-5}$, not only to take into account that vertical diffusion in the ocean is small (Ledwell et al. 1993), but also to ensure that vertical mixing between gravity currents and the ambient fluid takes place by eddy-induced mixing and entrainment and not by diffusion. As long as r is less than 10^{-3}, the results are quite insensitive to its value. The horizontal eddy viscosity ν_x is controlled by the model resolution and by the fastest signal in the system, the speed of the gravity current. A constant viscosity $\nu_x = 7$ m² s⁻¹ and diffusivity $K_x = 1$ m² s⁻¹ are used in the experiments, leading to a Prandtl number Pr = 7.

The boundary conditions applied to the system of equations (2)–(4) are as follows. At the surface, $\psi = \partial S/\partial z = 0$ and free slip; at the bottom, $\psi = \partial S/\partial z = 0$ and no slip; at the left and right boundaries, $\partial\psi/\partial x = \partial S/\partial x = 0$. The specification of $\psi = 0$ at the surface and bottom imposes zero net transport, thus creating a return surface flow in response to the descending gravity current. This is justified by the fact that strong return flows are observed above oceanic overflows (Baringer and Price 1997b). Sensitivity studies were conducted by increasing the total fluid depth from 1000 to 1200 m, and then to 1600 m (or, equivalently, the ratio of the thickness of the inflow to the overlying fluid is decreased from 1/2 to 1/8). This effectively reduces the speed of the surface current. The results were found to be quite insensitive to these changes.

While some of the observed overflows exhibit significant seasonal variability, or are even shut off completely at times (e.g., the Red Sea overflow, Murray and Johns 1997), the time scale of such variability (seasonal time scale) is much longer than the time that it takes for gravity currents to develop and reach a quasi equilibrium (typically on the order of hours). Therefore, the constant-buoyancy representation is applicable at least

TABLE 2. List of the expts 1–9.

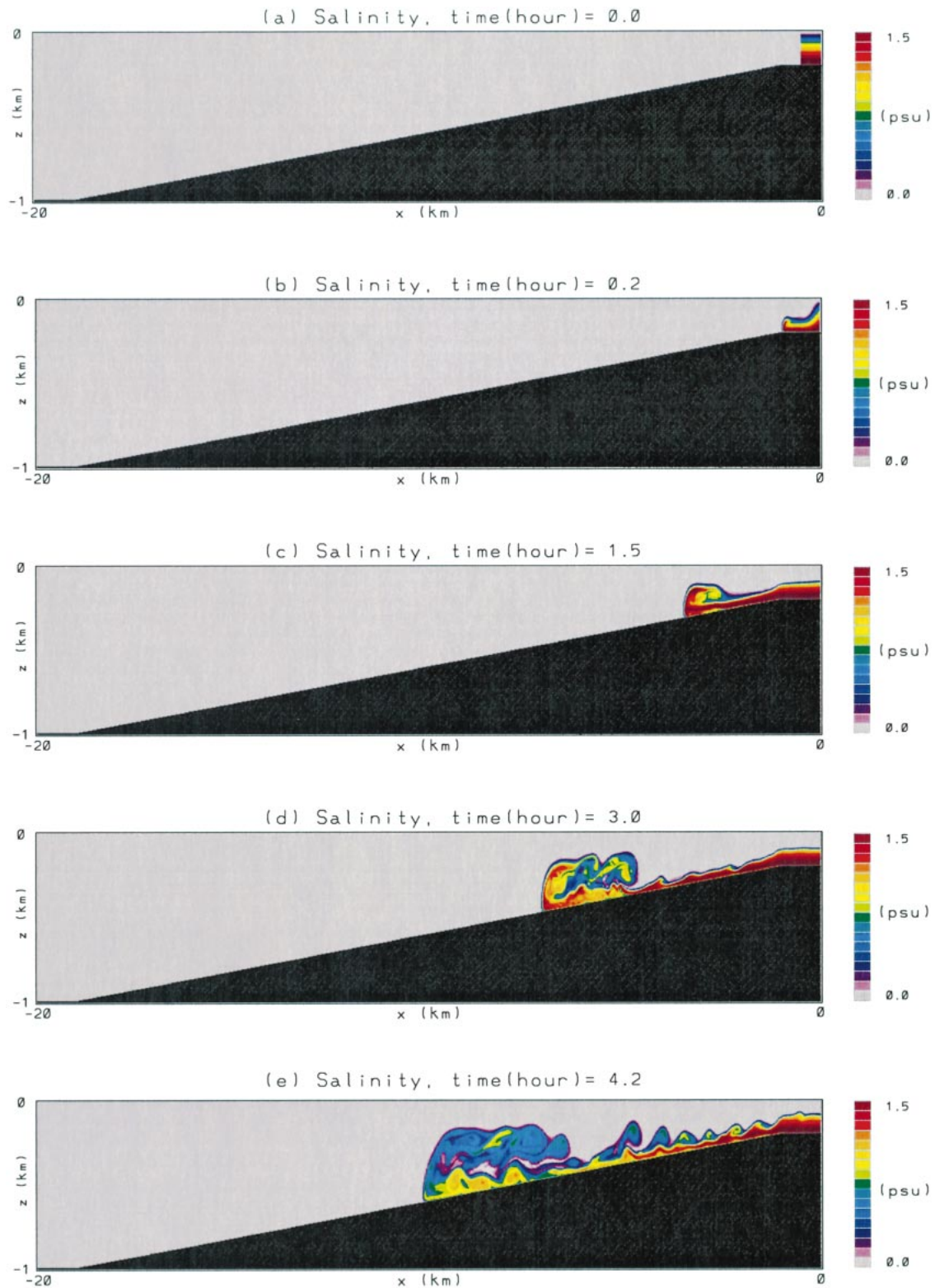|	Expt								
	1	2	3	4	5	6	7	8	9
ΔS (psu)	3.0	3.0	3.0	1.5	1.5	1.5	0.5	0.5	0.5
Slope angle θ (deg)	1.0	2.5	5.0	1.0	2.5	5.0	1.0	2.5	5.0

FIG. 1. Evolution of the simulated bottom density current as a function of time in expt 5 ($\Delta S = 1.5$ psu and $\theta = 2.5°$). Salinity distribution at (a) $t = 0$, (b) $t = 0.2$ h, (c) $t = 1.5$ h, (d) $t = 3.0$ h, and (e) $t = 4.2$ h.
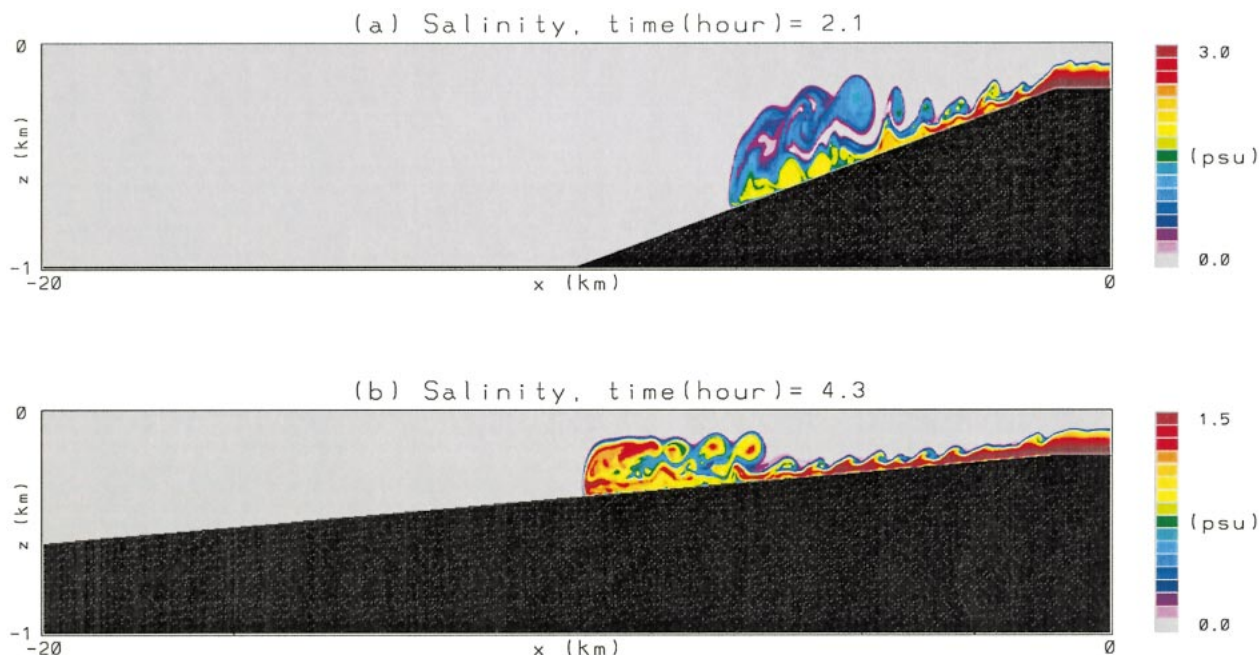
FIG. 2. Snapshots of the salinity distribution in (a) expt 3 ($\Delta S = 3.0$ psu and $\theta = 5°$) and (b) expt 4 ($\Delta S = 1.5$ psu and $\theta = 1°$).

over a timescale of days to weeks. In the model, the constant-buoyancy condition is provided by a small amount of fluid initially placed at the right upper corner of the domain (a simple representation of the "strait"; Fig. 1a), such that the salinity (density) input via the relaxation term on the rhs of (4) provides a constant buoyancy flux over a timescale much shorter than the time that it takes the density current to travel across the domain. The relaxation coefficient k has a value of (6 h)$^{-1}$ in the plateau of the strait and $k = 0$ elsewhere. The results were found to be insensitive to the relaxation frequency. The relaxation salinity value is $S^F = \Delta S$.

4. Effects of the bottom slope angle and input buoyancy flux

In this section, we determine the speed of advance of gravity currents as a function of buoyancy flux and bottom slope and then compare our results to those obtained from theory and laboratory experiments.

a. Qualitative comparison with laboratory experiments

The typical evolution of the modeled bottom density currents is depicted in Fig. 1 for experiment 5 ($\Delta S = 1.5$ psu, $\theta = 2.5°$). When the small amount of dense fluid is released at the strait (Fig. 1a), the initial development of the system is that of the so-called lock-exchange flow (e.g., Keulegan 1958; Simpson 1987) in which the lighter fluid remains on top and exits the domain through the open boundary and the denser fluid

sinks to the bottom and propagates downslope (Fig. 1b). The dense gravity current quickly reaches a constant rate of supply at the strait and develops a characteristic "head" at the leading edge of the current (Fig. 1c). The head is half of a dipolar vortex, which is a generic flow pattern that tends to form in two-dimensional systems via the self-organization of the flow (e.g., Flierl et al. 1981; Nielsen and Rasmussen 1996) and which corresponds to the most probable equilibrium state maximizing entropy (Smith 1991). In three dimensions, this feature is observed as "caps" on top of vertical plumes (Turner 1962). Initially, the gravity current is stable, but after 3 h and over a distance of about 7 km down the slope, the head becomes unstable, exhibiting breaking waves and intense mixing (Fig. 1d). There is a complicated shifting pattern of lobes and clefts caused by the gravitational instability of less dense fluid which is overrun by the nose of the current. The trailing current, the "tail," is marginally stable at this point in time, displaying only some patterns of waves, but later (4.2 h; Fig. 1e) the instability near the top of the tail leads to a rolling up of the density interface in lumped vortices separated by a characteristic length scale. This behavior is clearly indicative of the Kelvin–Helmholtz instability in which waves made up of fluid from the current entrap the ambient fluid (e.g., Corcos and Sherman 1984). The thickness of the tail is typically 100–200 m, in approximate agreement with the thickness of oceanic bottom density currents (Price and Yang 1998). The head grows and is diluted as the gravity current travels down the slope, due to entrainment of fresh ambient fluid (quantified in section 5). These general characteristics are
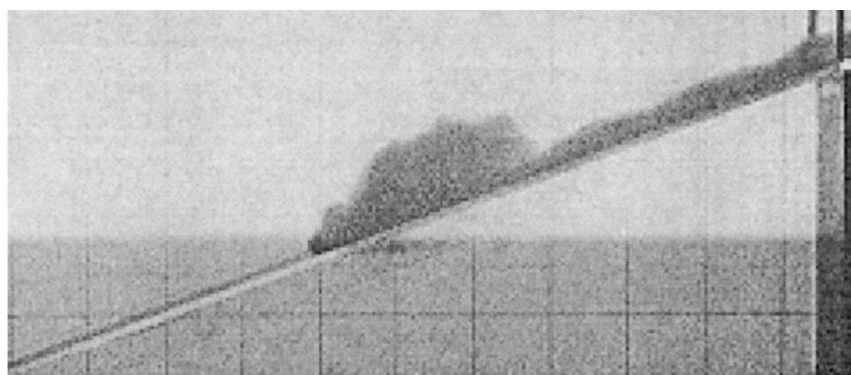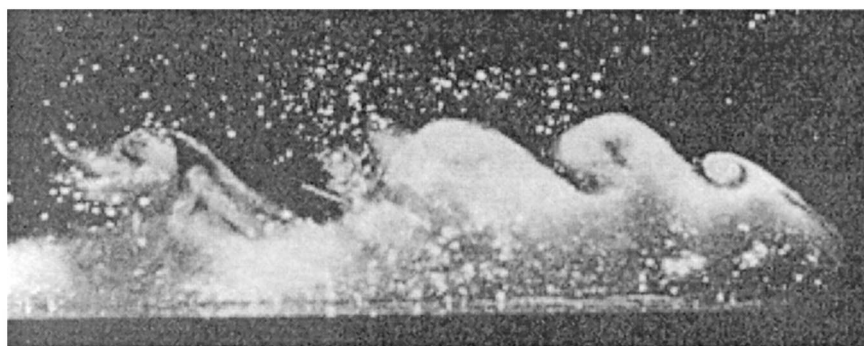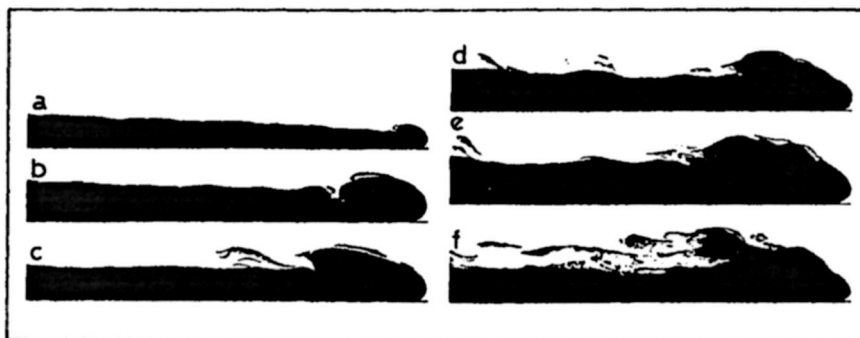
FIG. 3. Examples of laboratory gravity currents. (upper panel) Profiles of the head of horizontal gravity currents for increasing buoyancy flux (a)–(f), from Simpson (1982). (middle panel) Horizontal density current from Simpson (1969). (lower panel) Gravity current descending a ramp from Monaghan et al. (1999).

exhibited by all of experiments 1–9, as seen also from the snapshots of the salinity distribution in two other experiments depicted in Fig. 2.

Several examples of gravity currents from laboratory experiments are shown in Fig. 3 to provide a qualitative reference for our results. As in the numerically simulated gravity currents, the laboratory experiments exhibit the characteristic ''head'' that develops at the lead-ing edge of the current both on flat and inclined planes (Fig. 3, top and bottom panels, respectively) and mixing that takes place by the Kelvin–Helmholtz instability (Fig. 3, middle panel). Not only do the simulated gravity currents have different physical parameters from those in laboratory experiments, but the ratio of the spatial scales of simulated and laboratory gravity currents is also approximately $O(10^4$–$10^5)$.
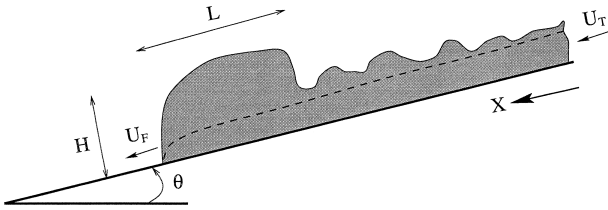
FIG. 4. Schematic illustration of the bottom gravity current on a slope with angle θ, downslope direction X, head height H, head length L, descent speed U_F, and tail speed U_T. The shaded area indicates the total area of the dense current A_{total}. The area remaining below the dashed line indicates the area in the absence of entrainment A_0, as defined in section 5c.

b. Comparison of the speed of descent with laboratory results

In order to conduct a quantitative comparison with laboratory experiments, the speed of descent of gravity currents for all numerical experiments is calculated by tracking the salinity front (Fig. 4). Britter and Linden (1980) found from theory and laboratory experiments that the head of density currents travels at a constant speed, U_F, proportional to the 1/3 power of buoyancy flux per unit width, defined as

$$B \equiv g'Q, \tag{5}$$

where $g' = g(\Delta\rho/\rho_0)$ (or $g' = g\beta\Delta S$ in expts 1–9) is the reduced gravity and $Q \equiv hU$ is the volume flux per unit width, with h and U being the average thickness and speed of the current at the input location. In the context of the present model, $Q = \psi_{\text{in}}$, where ψ_{in} is the maximum streamfunction value at the input location (the strait).

Figure 5 shows the ratio $U_F/B^{1/3}$ as a function of distance down the sloping bottom for all experiments. This scatterplot indicates that the numerical experiments are in agreement with the theoretical and laboratory results of Britter and Linden (1980) in that $U_F/B^{1/3}$ is approx-

imately constant for simulated gravity currents and is empirically expressed by

$$\frac{U_F}{B^{1/3}} = 1.05 \pm 0.1. \tag{6}$$

This result is in reasonable agreement with that of Britter and Linden (1980), who found $U_F/B^{1/3} = 1.5 \pm 0.2$, and is in excellent agreement with recent measurements by Monaghan et al. (1999), who reported $U_F/B^{1/3} = 1.0 \pm 0.1$.

These results are also in agreement with the observations of Ellison and Turner (1959), who concluded that the mean velocity of the gravity currents was independent of the downstream distance to the source. Figure 6 depicts the head speed as a function of distance for all experiments and shows that simulated density currents quickly attain an approximately constant speed of descent.

Laboratory experiments of gravity currents also show that the speed of descent remains roughly constant when the slope angle is varied. To explain this behavior, Britter and Linden (1980) surmised that the increase in the gravitational force due to greater slope angle is compensated by buoyancy gain due to increased entrainment both to the head and the tail. This effect produces an increased retarding force on the current as momentum is imparted to the entrained fluid. Therefore, the entrainment of ambient fluid into the gravity current must be represented in order to simulate the insensitivity of the descent speed to variations in θ. Figure 6 also shows clearly the grouping of head speed according to the salinity differences:

$$U_F \approx \begin{cases} 0.38 \text{ m s}^{-1} & \text{for } \Delta S = 0.5 \text{ psu} \\ 0.65 \text{ m s}^{-1} & \text{for } \Delta S = 1.5 \text{ psu} \\ 0.95 \text{ m s}^{-1} & \text{for } \Delta S = 3.0 \text{ psu.} \end{cases} \tag{7}$$

The experiments with a greater buoyancy flux (those with $\Delta S = 3.0$ psu) show higher variability in descent
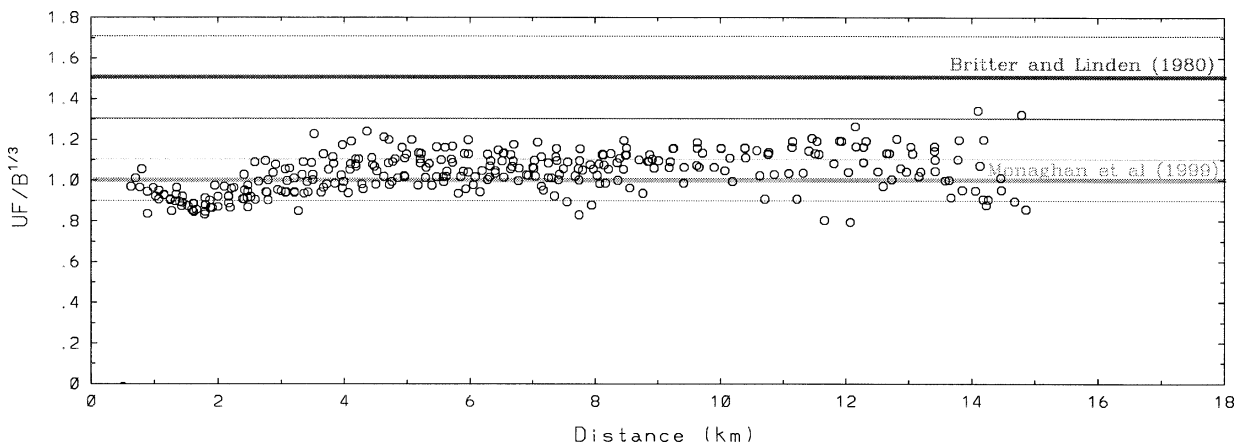

FIG. 5. The ratio of descent speed to buoyancy flux to the 1/3 power, $U_F/B^{1/3}$, vs distance for expts 1–9. Corresponding laboratory results from Britter and Linden (1980) and Mohaghan et al. (1999) are shown. Thick lines mark the mean value and thin lines indicate the range.
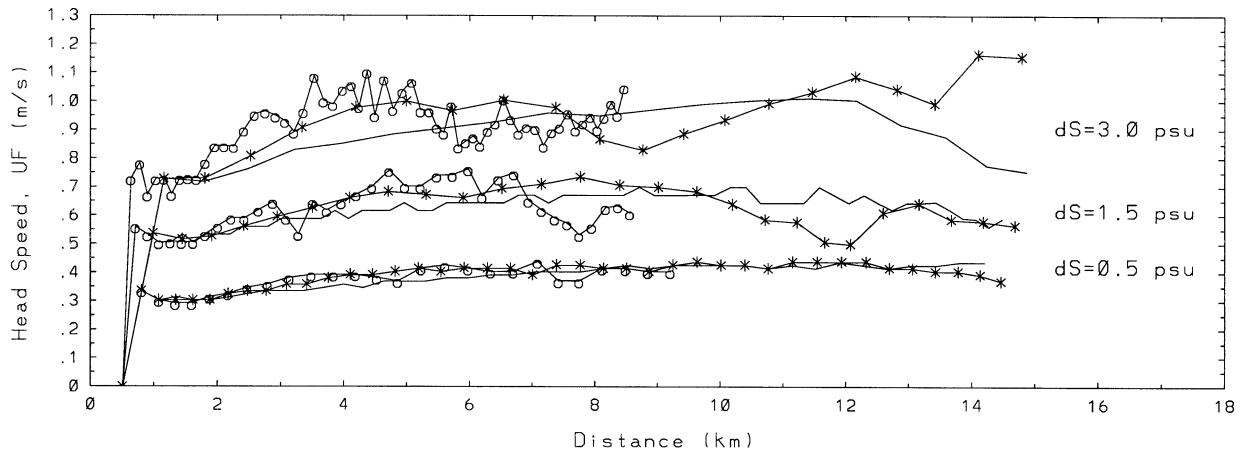
FIG. 6. Descent speed U_F (m s^{-1}) vs distance ($\theta = 1°$: solid line, $\theta = 2.5°$: line with asterisk symbols, $\theta = 5°$: line with circle symbols). Note that U_F is approximately independent of the bottom slope angle.

speed due to more vigorous and variable entrainment to the head, whereas those with a smaller buoyancy flux (e.g., those with $\Delta S = 0.5$ psu) exhibit less fluctuation. In general, however, the descent speed remains constant in the statistical sense when the slope angle is changed, in agreement with laboratory results.

The ratio of the head speed to that of the tail is an indicator of the slowing of the downward motion due to the entrainment of ambient fluid into the head, which increases as the gravity current flows down the slope. The tail speed, U_T, is calculated by taking a suitable sampling near the source,

$$U_T \equiv \frac{1}{(x_2 - x_1)(z_0 - z_b)} \int_{x_1}^{x_2} - \psi[x, z_0(x)] \, dx, \quad (8)$$

where $z_b(x)$ is the bottom depth, $z_0(x)$ is the depth at which the horizontal velocity becomes zero before reversing, and noting that $u = -\partial\psi/\partial z$ and $\psi[x, z_b(x)] = 0$. The interval $x_1 = -18$ km and $x_2 = -16$ km is taken close to the source but far enough away for currents to

attain full speed. The head speed is calculated after the front of the current passes this interval. The ratio of the head speed to that of the tail as a function of distance covered by the front is shown in Fig. 7 for experiments 1–9. Clearly, $U_F/U_T < 1$, or more quantitatively,

$$\frac{U_F}{U_T} = 0.74 \pm 0.07, \quad (9)$$

which indicates that the front of the density current moves slower than the tail due to momentum and buoyancy exchange with the ambient fluid. Therefore, the head volume increases not only due to entrainment of ambient fluid but also due to accumulation of the fluid coming from behind. The result (9) is within the range of laboratory values: Ellison and Turner (1959) reported $U_F/U_T \approx 0.61$–0.69 (depending on the slope angle), while Simpson and Britter (1979) measured $U_F/U_T \approx 0.85$. Since the entrainment drag acting on the head decreases with slope angle, U_F/U_T is inversely related to slope angle. Britter and Linden (1980) found that
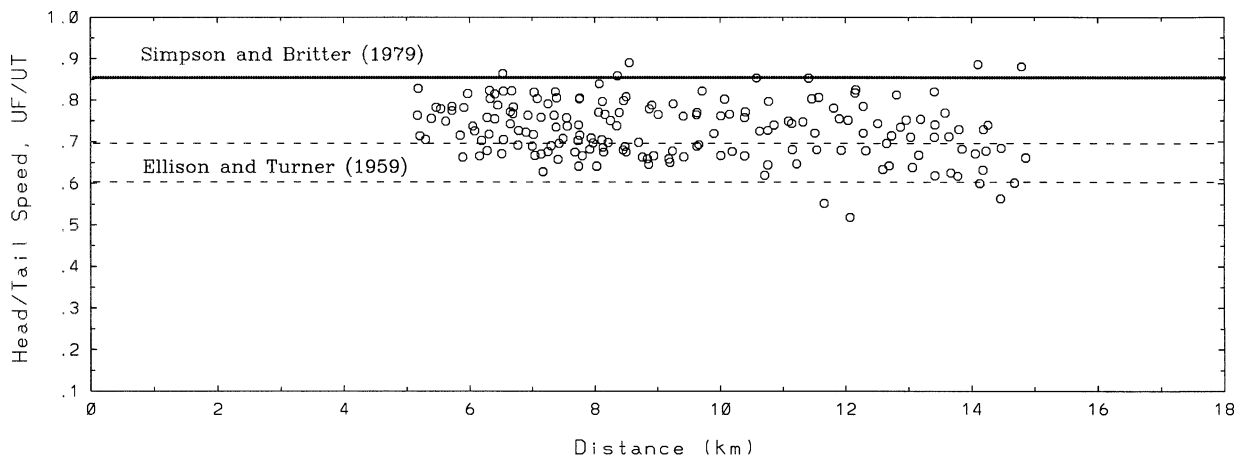

FIG. 7. The ratio of head speed to tail speed, U_F/U_T, as a function of the distance covered by the front, for expts 1–9. The solid line shows laboratory estimates by Simpson and Britter (1979), and the dashed lines indicate the range of values reported by Ellison and Turner (1959).
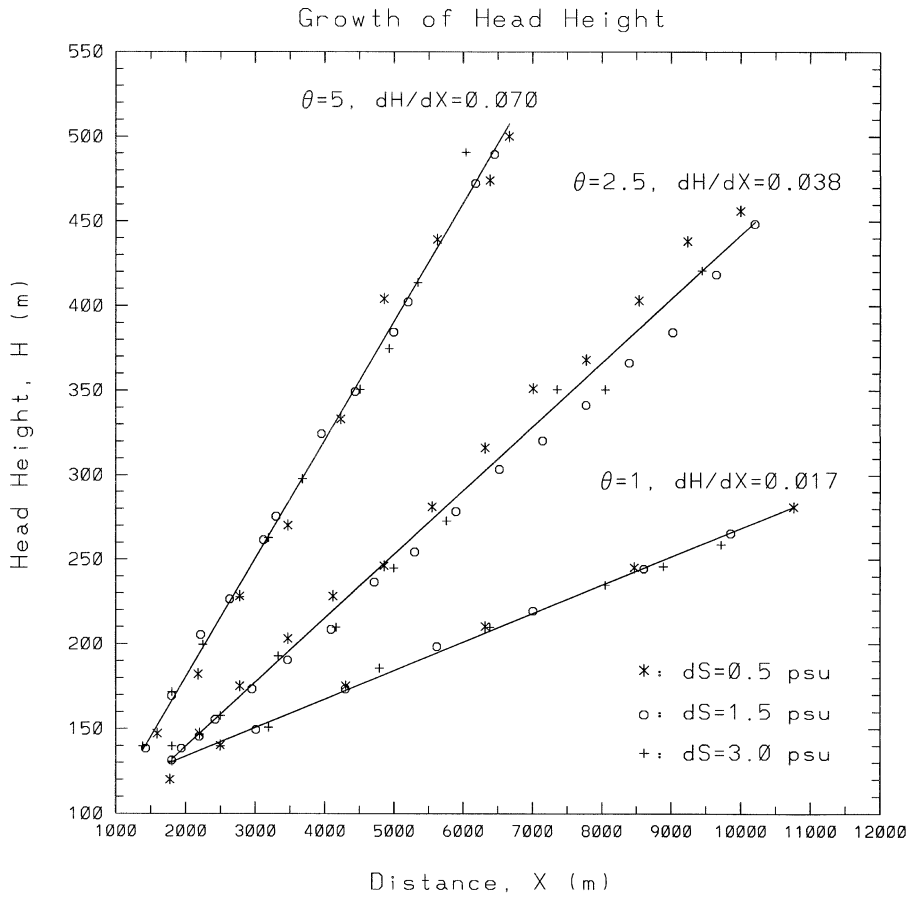
FIG. 8. Evolution of head height H as the gravity currents travel down the slope in expts 1–9. Data points in experiments with $\Delta S = 0.5$ psu, $\Delta S = 1.5$ psu, and $\Delta S = 3.0$ psu are marked with asterisks, circles, and plus signs respectively. Note the grouping of the growth rate according to slope angle θ, leading to $dH/dX \approx 0.017$ for $\theta = 1°$, $dH/dX \approx 0.038$ for $\theta = 2.5°$, and $dH/dX \approx 0.070$ for $\theta = 5°$.

$U_F/U_T \rightarrow 0.6$ for large slope angles ($\theta \geq 30°$), and Middleton (1966) showed that $U_F/U_T \rightarrow 1$ at small angles.

c. Comparison of the rate of head growth with laboratory results

Laboratory experiments by Ellison and Turner (1959), Britter and Linden (1980), and Monaghan et al. (1999) show that the rate of change of thickness of the head H with distance down the slope X is given by

$$\frac{dH}{dX} \approx 4 \times 10^{-3}\theta, \qquad (10)$$

where θ is in degrees.

In order to quantify the rate of change of H with distance X in the present numerical simulations, the thickness of the head is estimated from all experiments manually, by plotting the salinity distribution typically every 0.5 km of propagation distance. Since the characteristic head does not always remain coherent over time, the results presented in this section were evaluated

during the evolution of the boundary current over the first half of the domain. The results for dH/dX are shown in Fig. 8, which indicates that the rate of change is approximately independent of ΔS, and clearly exhibits a grouping according to the slope angle θ as well as a constant growth rate. A least squares approximation to the data points yields

$$\frac{dH}{dX} \approx \begin{cases} 0.017 & \text{for } \theta = 1° \\ 0.038 & \text{for } \theta = 2.5° \\ 0.070 & \text{for } \theta = 5°. \end{cases} \qquad (11)$$

The result (11) can be approximated as

$$\frac{dH}{dX} \approx 13 \times 10^{-3}\theta. \qquad (12)$$

Both (10) and (12) indicate that the simulations are able to capture the constant rate of growth of H with X, the independence of dH/dX from ΔS, and its linear dependence on θ correctly. However, dH/dX is overestimated by a factor of 3 when compared to the laboratory results. We surmise that this is due to the two-
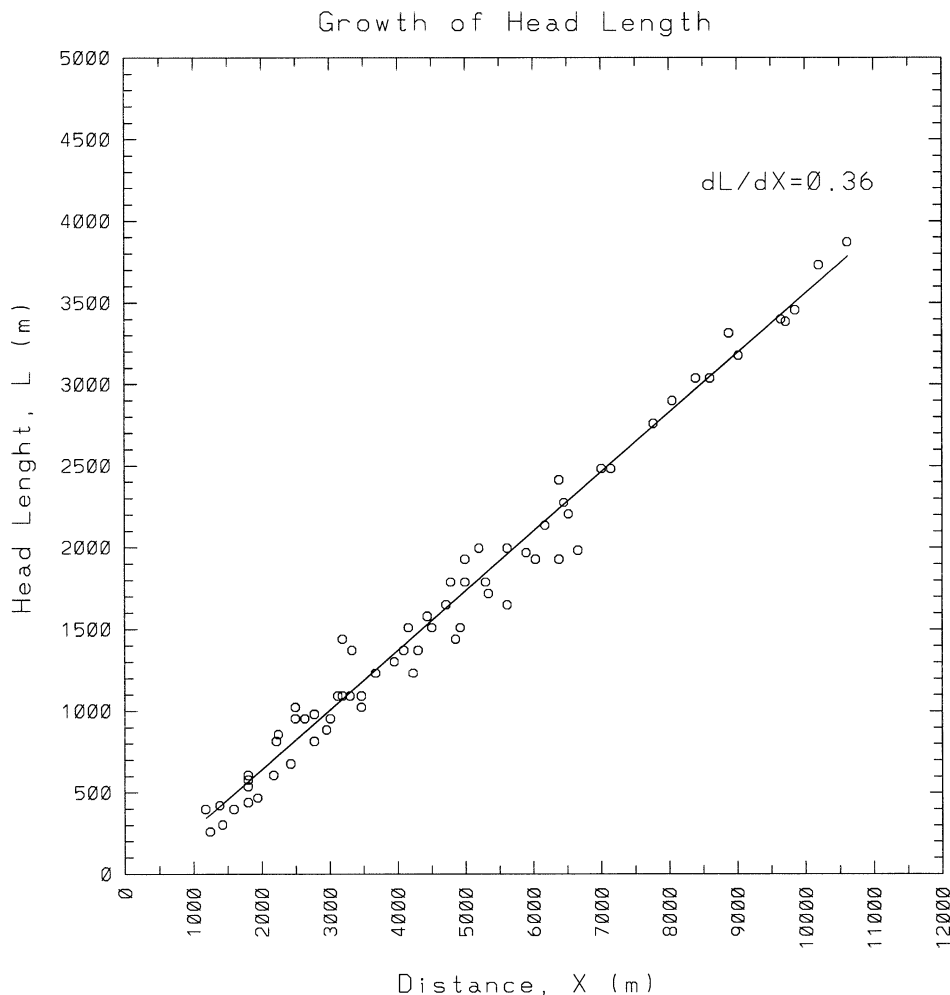
FIG. 9. Evolution of head length L as the gravity currents travel down the slope in expts 1–9. Data points are marked with open circles. The least squares approximation to data indicates $dL/dX \approx 0.36$.

dimensional nature of the solution, which does not allow for lateral spreading and widening of the current as it flows downslope. Turner (1986) reports that the spread of the head can be much larger than that of the plume behind. In the laboratory experiments, the drag exerted by the surrounding fluid induces the spreading and reduces the head growth. One can also estimate from the numerical experiments the length of the head. The results are plotted in Fig. 9 for experiments 1–9. The fit shows that

$$\frac{dL}{dX} \approx 0.36, \qquad (13)$$

hence a constant rate of change of L with X, independent of θ and ΔS within the parameter range of the experiments. There are no laboratory measurements available for comparison but, since dH/dX is overestimated in the numerical experiments, it is likely that dL/dX is also overestimated for the same reasons.

Britter and Linden (1980) discuss the aspect ratio H/L for several experiments at different slope angles. The smallest angle in Britter and Linden (1980) is 5°, so we looked at the aspect ratio H/L in experiments 3, 6, and 9, the experiments conducted on a slope with an angle of 5°. The aspect ratio is shown as a function of distance X in Fig. 10. After a short distance down the slope (approximately 1 km), the aspect ratio from these experiments oscillates around a mean value of

$$\frac{H}{L} \approx 0.25 \quad \text{for } \theta = 5°, \qquad (14)$$

which is in good agreement with the observations of Wood (1965) as reported by Britter and Linden (1980).

5. Entrainment

In the previous section, we showed that the numerical simulations compare well with laboratory measurements and that the laboratory results are valid on geophysical
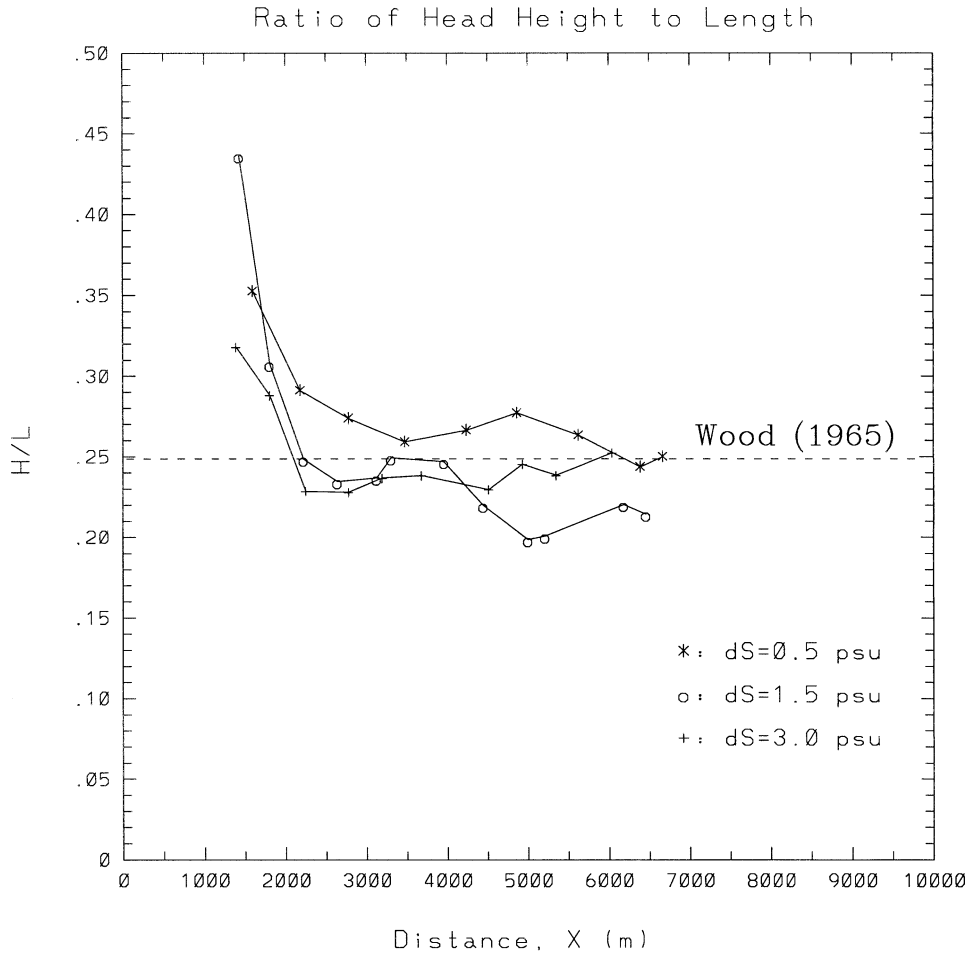
Ratio of Head Height to Length

FIG. 10. The ratio of head height to head length H/L as a function of distance in expt 3 ($\Delta S = 3$ psu, $\theta = 5°$, the line with plus signs), expt 6 ($\Delta S = 1.5$ psu, $\theta = 5°$, the line with open circles), and expt 9 ($\Delta S = 0.5$ psu, $\theta = 5°$, the line with asterisks). The dashed line indicates the laboratory result by Wood (1965) that $H/L \approx 0.25$ for gravity currents over a slope with $\theta = 5°$.

scales. We can now investigate in detail the characteristics of the mixing taking place between the simulated bottom gravity currents and the ambient fluid.

a. Qualitative analysis of entrainment

In order to visualize the nature of entrainment, 500 Lagrangian particles were released into the flow field in experiment 5 ($\Delta S = 1.5$ psu and $\theta = 2.5°$) between $t = 4.2$–4.8 h on a regular grid (horizontal spacing of 400 m or every 80 grid points and vertical spacing of 20 m or every 4 grid points). The trajectories are plotted in Fig. 11 (see the figure caption for further details). They indicate a clear distinction between the entrainment characteristics in the head and the trailing flow. In the head section, entrainment takes place by two mechanisms. First, the lighter fluid is displaced and lifted up by the front of the gravity current, and strong entrainment takes place into the head from behind.

Therefore, the head vortex carries fresh fluid from around the front to the rear of the head, and this entrainment in return leads to the growth of the head. This is in qualitative agreement with laboratory observations by Monaghan et al. (1999). A secondary type of entrainment into the head takes place by light fluid that cannot travel around the head, and is thus overrun by the oncoming gravity current. Since this fluid is lighter than the fluid in the head, it rises by gravitational instability and leads to additional mixing in the head. This can be seen in Fig. 11, near the bottom of the slope at approximately $x = -8$ km, and in laboratory experiments as well (e.g., Simpson and Britter 1979).

In the tail section, the formation of distinct vortices engulfs fluid from the ambient flow and enhances the transport of the density current. Most of the entrainment takes place in between the vortices. There is also a general tendency for these vortices to coalesce and form larger vortices via pairing (observed via movies of our
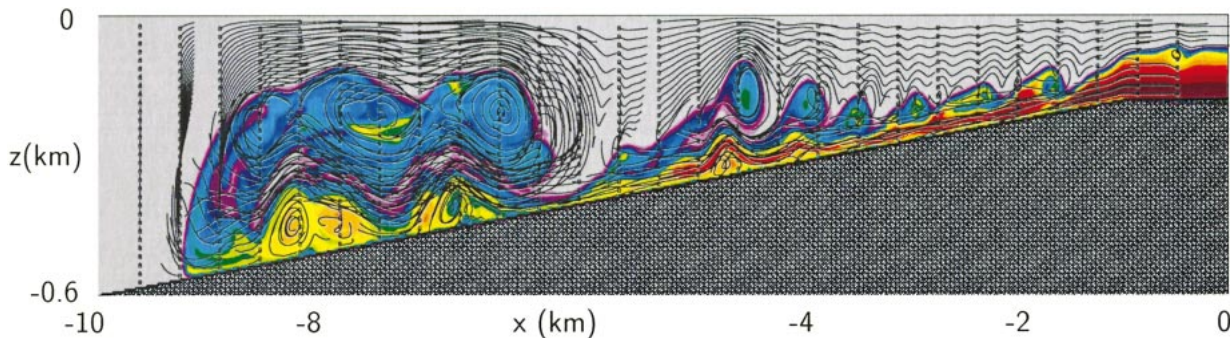
FIG. 11. Trajectories of approximately 500 Lagrangian particles released into the velocity field between $t = 4.2 - 4.8$ h in a regular array (with an horizontal spacing of 400 m or every 80 grid points, and a vertical spacing of 20 m or every 4 grid points) in expt 5 ($\Delta S = 1.5$ psu and $\theta = 2.5°$). Salinity field is plotted in the background at $t = 4.5$ h (refer to Fig. 1 for the colorbar).

numerical simulations). This is a well-documented be-havior of two-dimensional Kelvin–Helmholtz instability (e.g., Fig. 15 of Corcos and Sherman 1984).

b. Quantitative analysis of entrainment to the head and the tail

The entrainment in the head can be quantified fol-lowing the definition of Ellison and Turner (1959) and Turner (1986),

$$E_H \equiv \frac{dH}{dX}. \qquad (15)$$

The quantity dH/dX was calculated in section 4 for ex-periments 1–9 and the entrainment E_H is therefore given by (12).

The entrainment in the tail can be quantified following the definition of Morton et al. (1956),

$$E_T \equiv \frac{\overline{w}_E}{U_T}, \qquad (16)$$

where $\overline{w}_E$ is the entrainment velocity into the tail. The entrainment velocity is estimated from

$$\overline{w}_E \equiv \frac{\Delta\psi}{l}, \qquad (17)$$

where $\Delta\psi$ is the increase in the transport of the density current over the length of the tail section, l. Hence, $\overline{w}_e$ is the average net entrainment velocity into the tail (pos-itive downward). This definition of E_T is similar to the one defined by Turner (1986) as dh/dX, where h is the
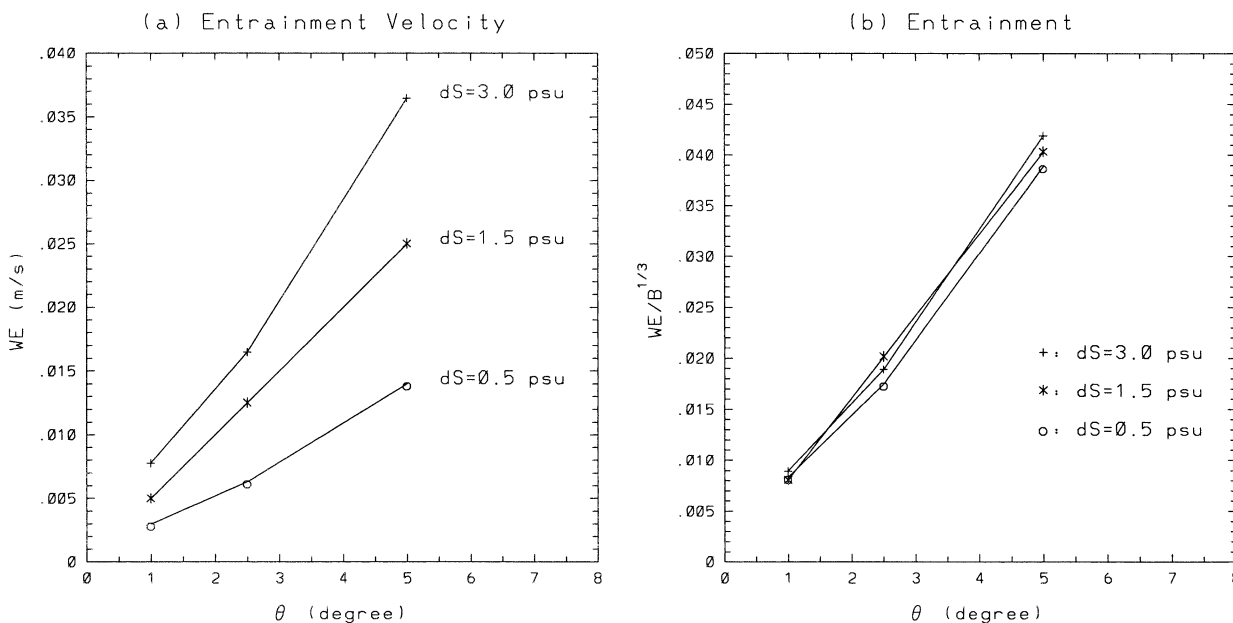

FIG. 12. (a) Entrainment velocity $\overline{w}_E$ in the tail section as a function of slope angle θ and salinity difference ΔS as estimated from expts 1–9. (b) As in (a) but for scaled parameter $\overline{w}_E/B^{1/3}$.
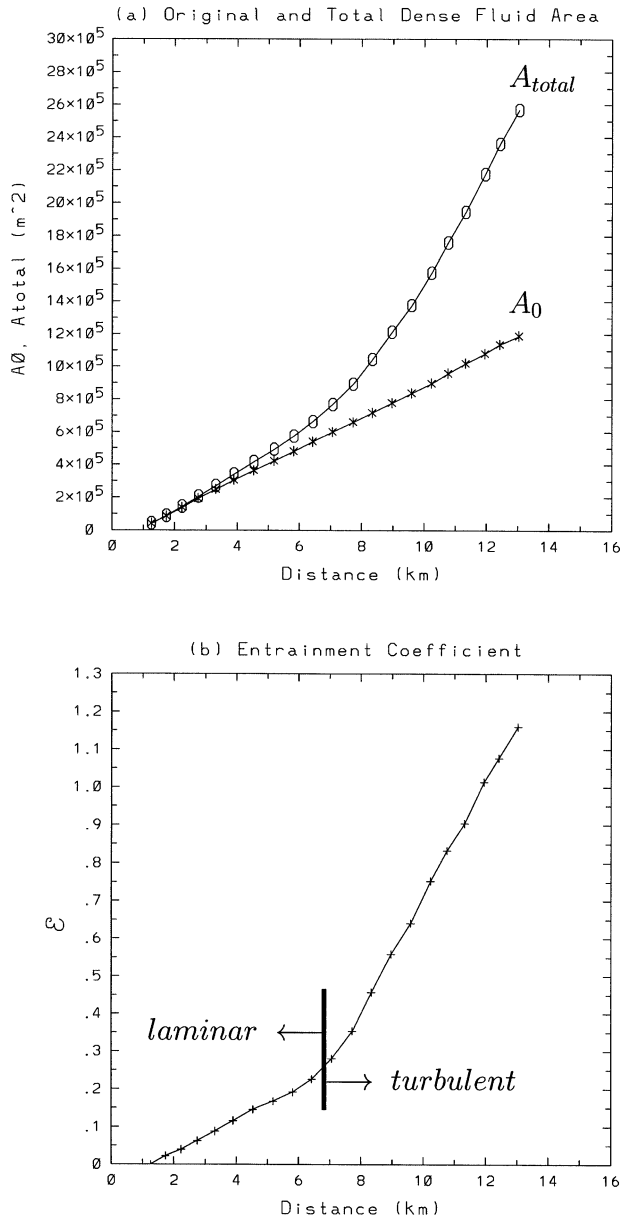
FIG. 13. (a) Original (supplied) dense fluid area A_0 and total (after mixing) dense fluid area A_{total} (in m²), and (b) entrainment coefficient E as a function of downslope distance X (in km) for Exp-5 ($\Delta S = 1.5$ psu and $\theta = 2.5°$). The sampling points are marked.

TABLE 3. Comparison of entrainment parameters based on laboratory experiments of Ellison and Turner (1959) (Turner 1986): E as given in eq. (20) vs expts. 1–9 in this study, E_T as given in Eq. (19) for $1° \leq \theta \leq 5°$.

1°	6×10^{-3}	5.6×10^{-3}	0.9
2.5°	7.5×10^{-3}	14×10^{-3}	1.9
5°	10×10^{-3}	28×10^{-3}	2.8

$$\frac{\overline{w}_E}{B^{1/3}} \approx 8 \times 10^{-3}\theta, \qquad (18)$$

for $1° \leq \theta \leq 5°$. This is in agreement with Fig. 5, which shows that the changes in slope angle are compensated by changes in the strength of the entrainment. Then, using the empirical relationships [(6) and (9), previously derived in section 4], $U_F/B^{1/3} \approx 1.05$ and $U_F/U_T \approx 0.74$, the entrainment in the tail can be quantified by

$$E_T \approx 5.6 \times 10^{-3} \theta. \qquad (19)$$

The entrainment parameter based on the laboratory experiments of Ellison and Turner (1959), as given by Turner (1986), is

$$E \approx (5 + \theta) \times 10^{-3}. \qquad (20)$$

A comparison of E to the entrainment parameter E_T of (19) is presented in Table 3. The observed and simulated parameters agree well for a slope angle $\theta = 1°$, but are overestimated in the numerical experiments by factors of 2 and 3 for $\theta = 2.5°$ and $5°$, respectively. The ratio of entrainment to the head and to the tail in experiments 1–9 can be calculated from (12) and (19) as

$$\frac{E_H}{E_T} \approx 2.3, \qquad (21)$$

which indicates that entrainment to the head is stronger than that to the tail.

Entrainment results presented in this section rely on the separation of head and tail, and these features become gradually less distinct from one another as the currents travel down the slope. The head loses its distinctive nature in some experiments, resembling that in Fig. 3, middle panel. Therefore, these results are restricted to a downslope distance of approximately 10 km for experiments with $\theta = 1°$ and $\theta = 2.5°$ and of approximately 5–6 km for experiments with $\theta = 5°$.

c. Total entrainment

The definitions of entrainment in the previous section [(15) and (16)] are valid only as long as the head and tail remain separate entities. This is not always the case since the head eventually merges with the tail as the head grows with downslope distance. In order to provide a better quantification of the total entrainment of ambient fluid into the gravity current, we define an unambiguous metric following Meleshko and Van Heijst (1995):

thickness of the tail, since $E_T = \Delta\psi/(U_T l) \approx \Delta h/\Delta X$ (assuming $\Delta\psi/U_T = \Delta h$ and $l = \Delta X$).

Figure 12a shows that the average net entrainment velocity $\overline{w}_E$ into the tail of density currents in experiments 1–9 increases with slope angle and salinity difference from the surrounding fluid. Using the characteristic speed scale $B^{1/3}$ given by the buoyancy flux, one can show that the curves in Fig. 12a collapse approximately on a single curve (Fig. 12b), which can be approximated by

(a) Laminar Entrainment, $\theta=1$

$d\mathcal{E}/dX=0.020$

*, dS=0.5 psu
o, dS=1.5 psu
+, dS=3.0 psu

(b) Laminar Entrainment, $\theta=2.5$

$d\mathcal{E}/dX=0.043$

*, dS=0.5 psu
o, dS=1.5 psu
+, dS=3.0 psu

(c) Laminar Entrainment, $\theta=5$

$d\mathcal{E}/dX=0.086$

*, dS=0.5 psu
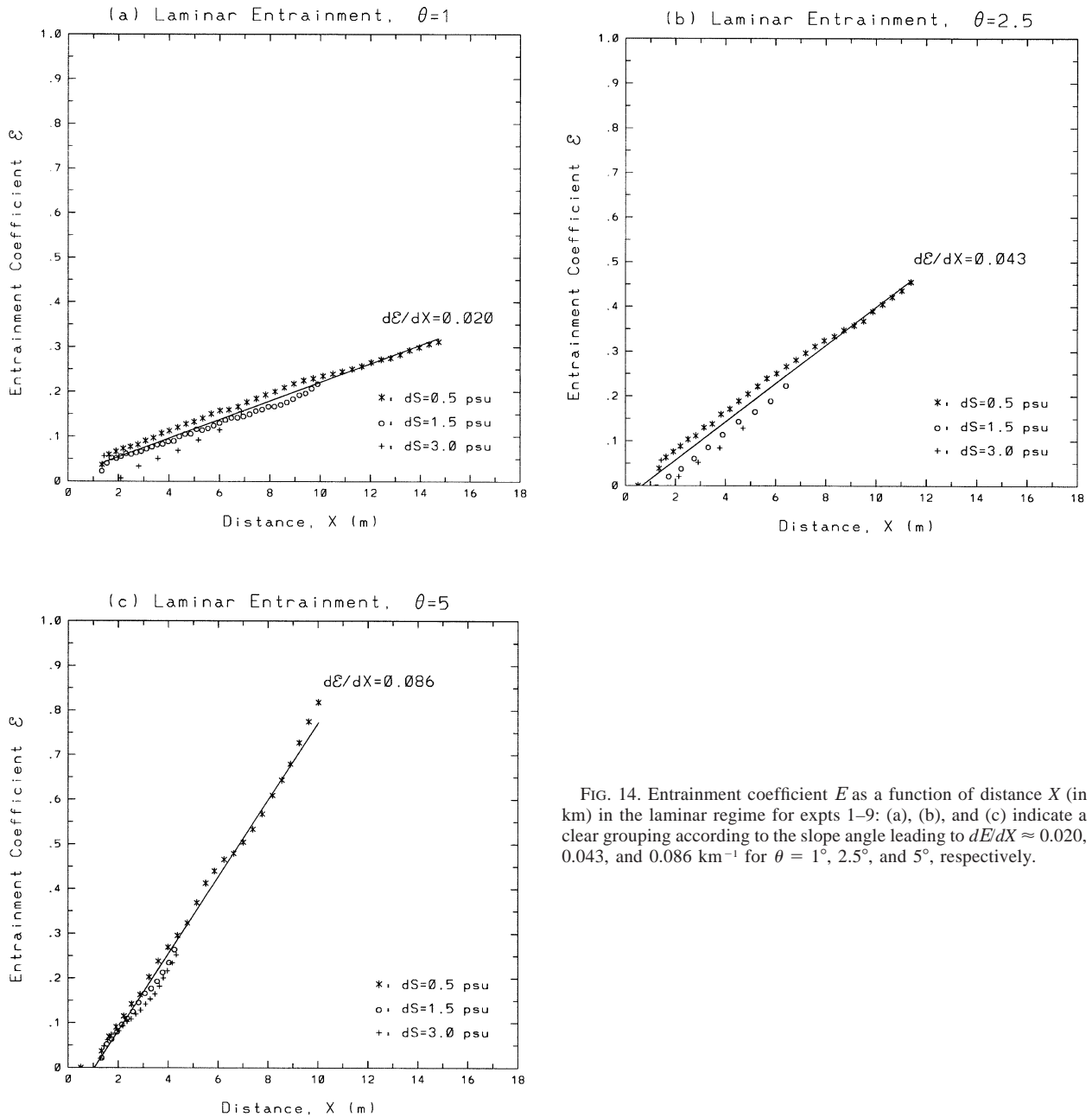o, dS=1.5 psu
+, dS=3.0 psu

FIG. 14. Entrainment coefficient E as a function of distance X (in km) in the laminar regime for expts 1–9: (a), (b), and (c) indicate a clear grouping according to the slope angle leading to $dE/dX \approx 0.020$, 0.043, and 0.086 km^{-1} for $\theta = 1°$, 2.5°, and 5°, respectively.

$$E \equiv \frac{A_{\text{total}} - A_0}{A_0}, \qquad (22)$$

where

$$A_0 = \int_0^t \int_0^h u(x_0, z, t) \, dz \, dt = \int_0^t \psi(x_0, h, t) \, dt \quad (23)$$

is the total volume per unit depth (area) of dense water that has entered the domain across x_0 with thickness h in the strait. In the absence of any entrainment, the total area that has entered the domain, A_0, would be equal to the total area of dense fluid within the domain, A_{total}.

Therefore, the entrainment coefficient $E = 0$ in the absence of mixing. When, however, there is entrainment of ambient fluid, the total area of the dense fluid inside the domain would be larger than the area that has actually entered through the boundary, $A_{\text{total}} > A_0$, and hence $E > 0$. For instance, $E = 1$ for 50% dilution of the density current or, in other words, the inflation of the area of dense fluid by a factor of 2.

The time evolutions of the original dense fluid area A_0, the total dense fluid area A_{total}, and the entrainment coefficient E are illustrated in Fig. 13 for experiment 5 ($\Delta S = 1.5$ psu and $\theta = 2.5°$). These quantities are shown

as a function of the downstream distance X using the linear relationship between distance and time resulting from the constant descent speed (section 4). The amount of dense water entering the domain, A_0, increases linearly with X (Fig. 13a) because of the constant rate of volume/depth flux at the strait. For the first 5–6 km down the slope, there is no significant difference between A_0 and A_{total}, indicating small entrainment of ambient fluid to the gravity current. But at $X \approx 7$ km, A_{total} starts to deviate significantly from A_0, indicating the occurence of high entrainment. The transition point at $X \approx 7$ km coincides with the onset of instabilities in the gravity current (Fig. 1d). The quadratic increase of A_{total} with X is related to the increase in the thickness of the gravity current due to entrainment by shear instability, in addition to the increase in its length. The variation of the entrainment coefficient E as a function of X is shown in Fig. 13b, which clearly indicates two distinct regimes of entrainment. In the first regime (1 km $< X <$ 7 km), the linear increase E with X is due to the formation of the characteristic head vortex (e.g., Fig. 1c). This regime is denoted as the *laminar entrainment regime*. Then, a rapid transition to the second regime takes place ($X >$ 7 km) in which E also increases linearly with X, but at a much higher rate than in the first regime. This regime is denoted as the *turbulent entrainment regime*. Figure 13b also indicates that at $X \approx 12$ km, $E \approx 1$; that is, the original area of the gravity current is doubled due to entrainment of ambient fluid.

The entrainment coefficient E as a function of the downstream distance X for the laminar entrainment regime is shown for all experiments in Fig. 14. There is a clear dependence on the slope angle θ. In general, dE/dX, the rate at which the gravity plume is diluted over distance, increases with θ, or quantitatively,

$$\left(\frac{dE}{dX}\right)_{laminar} \approx \begin{cases} 2.0 \times 10^{-5} \text{ m}^{-1} & \text{for } \theta = 1° \\ 4.3 \times 10^{-5} \text{ m}^{-1} & \text{for } \theta = 2.5° \\ 8.6 \times 10^{-5} \text{ m}^{-1} & \text{for } \theta = 5°. \end{cases} \quad (24)$$

The result (24) can be approximated by

$$\left(\frac{dE}{dX}\right)_{laminar} \approx 1.7 \times 10^{-5} \text{ (m}^{-1})\theta. \quad (25)$$

The entrainment coefficient E as a function of downstream distance X in the turbulent entrainment regime is shown for all experiments in Fig. 15. As in the laminar regime, dE/dX increases with slope angle θ. Also, as ΔS increases, the transition to turbulence takes place over a shorter distance X (i.e., the curves representing experiments with $\Delta S =$ 3.0 psu are to the left of those for $\Delta S =$ 1.5 psu). The curves indicate that the bottom gravity currents on higher slope angles make a transition to turbulent entrainment over a shorter distance than those with smaller slope angles. Two experiments do not exhibit any turbulent entrainment: experiment 7 (ΔS = 0.5 psu and $\theta =$ 1°), which remains laminar (smallest

ΔS and slope), and experiment 9 ($\Delta S = 0.5$ psu and $\theta = 5°$), which does not have enough distance for the transition to turbulence to occur.

The quantitative results for the turbulent entrainment regime are:

$$\left(\frac{dE}{dX}\right)_{turbulent} \approx \begin{cases} 11.3 \times 10^{-5} \text{ m}^{-1} & \text{for } \theta = 1° \\ 15.7 \times 10^{-5} \text{ m}^{-1} & \text{for } \theta = 2.5° \\ 21.1 \times 10^{-5} \text{ m}^{-1} & \text{for } \theta = 5° \end{cases} \quad (26)$$

or

$$\left(\frac{dE}{dX}\right)_{turbulent} \approx 10 \times 10^{-5} \text{ (m}^{-1})\sqrt{\theta}. \quad (27)$$

A comparison of the laminar and turbulent entrainment rates, (25) and (27), shows that (i) the rate of increase of turbulent entrainment with distance is greater than that for the laminar entrainment and (ii) the turbulent entrainment regime exhibits less sensitivity to the slope angle θ than the laminar entrainment regime ($dE/dX \sim \sqrt{\theta}$ vs $dE/dX \sim \theta$).

The rate of change of E with time can be estimated using $dX/dt \approx U_F$ and the ratio $U_F/B^{1/3}$ (6). For the turbulent entrainment regime, the rate of change of the entrainment coefficient can then be written as

$$\left(\frac{dE}{dt}\right)_{turbulent} \approx 10^{-4} \text{ (m}^{-1})\sqrt{\theta}B^{1/3}. \quad (28)$$

This means that, for example, the time scale for a gravity current with $\Delta S = 1.5$ psu on a slope of 1° to double its volume/depth by turbulent entrainment is approximately 4 h.

The turbulent entrainment relationships (27) and (28) quantify the mixing time and space scales of bottom gravity currents as a function of the basic parameters of the system, that is, the slope angle θ and the buoyancy flux B, which are in general quite well known for most oceanographic flows. Consequently, these relationships can be useful in developing parameterizations of mixing of bottom gravity currents.

6. Summary and discussion

In light of recent studies demonstrating that the large-scale thermohaline circulation in ocean general circulation models is strongly controlled by the details of mixing of the overflows across the Greenland–Scotland region (DYNAMO Group 1997; Willebrand et al. 2001) and that the entrainment of Atlantic water into the Mediterranean overflow may lead to the formation of basin-scale currents such as the Azores Current (Jia 2000) and Azores Countercurrent (Özgökmen et al. 2001), the detailed structure of the start-up phase of bottom gravity currents in a nonrotating and homogeneous environment is explored by using a two-dimensional, nonhydrostatic model. The primary characteristic of the numerical simulations is that the Kelvin–Helmholtz instability, the
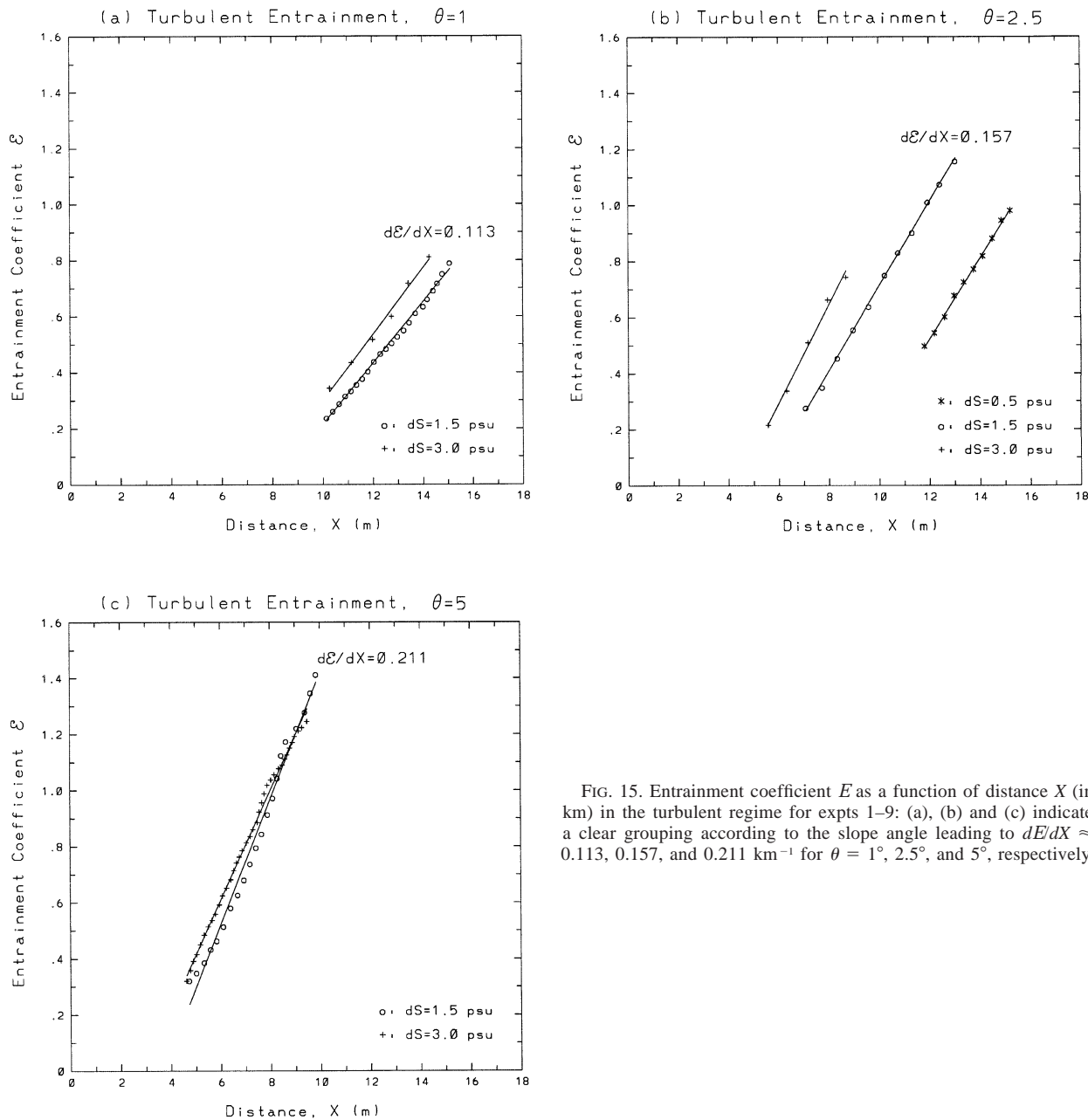
FIG. 15. Entrainment coefficient E as a function of distance X (in km) in the turbulent regime for expts 1–9: (a), (b) and (c) indicate a clear grouping according to the slope angle leading to $dE/dX \approx$ 0.113, 0.157, and 0.211 km^{-1} for $\theta = 1°$, 2.5°, and 5°, respectively.

main mechanism of mixing of bottom gravity currents, is explicitly captured due to high model resolution.

Two questions were addressed: (i) are the results obtained in laboratory experiments valid for geophysical scales and parameters and (ii) can we quantify and parameterize the details of the mixing? A series of numerical experiments were analyzed for bottom gravity currents, with density contrasts and slope angles representative of oceanic overflows.

As in the laboratory experiments, the numerical simulations exhibit a characteristic head at the leading edge of the currents and distinct lumped vortices along the density interface between the ambient fluid and the tail

of gravity currents. Quantitatively, as for the laboratory experiments, the speed of descent of gravity currents is determined by the buoyancy flux at the input location, $U_F \approx B^{1/3}$. The increase in gravitational force is compensated by increased entrainment when the slope angle is increased. The tail speed is approximately 33% higher than the head speed, leading to accumulation of fluid toward the leading edge, hence to the growth of the characteristic head with distance. Overall, most of the quantitative measures performed in the laboratory experiments can be carried over to the numerical experiments, despite the different scales and parameters.

In the numerical experiments, the characteristics of

mixing between the gravity currents and the ambient fluid can be analyzed in detail. Two different regimes of entrainment were identified by releasing Lagrangian particles into the flow field. The head of the gravity currents displaces and lifts the lighter fluid ahead, which is then entrained into the head from behind. In the tail section, Kelvin–Helmholtz vortices are generated and entrain fluid from the ambient flow. Both entrainment mechanisms are quantified according to conventional definitions and are found to depend only on the slope angle, in agreement with laboratory results. The entrainment in the head however is overestimated in the model when compared to the laboratory results. This is likely a consequence of the two-dimensional nature of the numerical simulations, which do not allow for any lateral spreading of the head.

In the numerical simulations, the head and the tail do not always remain as two distinct entities as the head grows and merges with the tail. A separate analysis of the entrainment into the head and tail is therefore not always possible, and a more general measure of the entrainment needs to be introduced. A simple but unambiguous metric for total entrainment was therefore introduced as the ratio of the volume increase in fluid denser than the background to the volume of fluid entering the domain. In the absence of any entrainment, there would be no increase in denser fluid, and therefore the entrainment coefficient would be equal to zero. The variation of this coefficient with respect to the distance covered by the descending gravity currents shows two different regimes of entrainment, laminar and turbulent. The former is due to the formation of the head vortex by the drag exerted by the fresh fluid ahead as the current starts its initial descent, and the latter begins with the transition to turbulence and is associated with shear instability. The entrainment in both regimes was quantified, and it was shown that the turbulent entrainment is much stronger than the laminar entrainment. The time evolution of the entrainment was found to be a function of the slope angle only, but with less sensitivity in the turbulent regime (proportional to $\sqrt{\theta}$ and θ, respectively). Finally, the timescale of turbulent mixing can be estimated as a function of main parameters of the system, that is, the buoyancy flux B and the slope angle θ.

Given the idealized nature of the experiments, we next address the implications of the various assumptions and simplifications and outline recommendations for future studies. First, the head of gravity currents is a feature of the start-up phase, and it is therefore not clear how it is relevant to geophysical overflows. Some overflows are approximately continuous, but it is known that the Red Sea overflow shuts off completely at the end of summer (Murray and Johns 1997). One would therefore expect the formation of a characteristic head when this overflow starts flowing again. Localized heads can be formed by high frequency fluctuations in the outflow buoyancy flux, such as tidal effects in the Mediterranean

overflow (e.g., Baschek and Send 1999). Localized heads can also be formed in regions of large variations in the topographic slope. These variations induce local deceleration/acceleration of the dense fluid. Second, the experiments exhibit continuous entrainment within the length of simulations. It needs to be explored whether entrainment would slow down or would totally shut off at some point in time, and this requires simulations in a much larger domain. More comprehensive entrainment relationships, such as Richardson number dependent entrainment criteria, may control the beginning and ending of turbulent entrainment. The effect of rotation should be investigated using a 3D model and a larger domain. Based on laboratory experiments, Griffiths and Hopfinger (1983) report that vertical mixing in the rotating case appears to be more vigorous than in the nonrotating case. Also, deflection of the current parallel to topographic contours will take place on scales larger than the radius of deformation. Additional factors need to be taken into account such as the effects of ambient stratification, continuous overflows, topographic features, etc. These will be topics of further investigation.

REFERENCES

Arakawa, A., 1966: Computational design for long-term numerical integration of the equations of fluid motion: Two dimensional incompressible flow. Part I. *J. Comput. Phys.,* **1,** 119–143.
Baringer, M. O., and J. F. Price, 1997a: Mixing and spreading of the Mediterranean outflow. *J. Phys. Oceanogr.,* **27,** 1654–1677.
——, and ——, 1997b: Momentum and energy balance of the Mediterranean outflow. *J. Phys. Oceanogr.,* **27,** 1678–1692.
Baschek, B., and U. Send, 1999: Analysis of flow and transport measurements in the Strait of Gibraltar. *Eos, Trans. Amer. Geophys. Union,* **80,** p. OS72.
Borenäs, K. M., and P. A. Lundberg, 1988: On the deep-water flow through the Faroe Bank Channel. *J. Geophys. Res.,* **93,** 1281–1292.
Britter, R. E., and J. E. Simpson, 1978: Experiments on the dynamics of a gravity current head. *J. Fluid Mech.,* **88,** 223–240.
——, and P. F. Linden, 1980: The motion of the front of a gravity current traveling down an incline. *J. Fluid Mech.,* **99,** 531–543.
Bryden, H. L., and T. H. Kinder, 1991: Steady two-layer exchange through the Strait of Gibraltar. *Deep-Sea Res.,* **38** (Suppl.), S445–S463.
Corcos, G. M., and F. S. Sherman, 1984: The mixing layer: Deterministic models of a turbulent flow. Part 1. Introduction and the two-dimensional flow. *J. Fluid Mech.,* **139,** 29–65.
Dickson, R. R., E. M. Gmitrowics, and A. J. Watson, 1990: Deep water renewal in the northern North Atlantic. *Nature,* **344,** 848–850.
DYNAMO Group, 1997: Simulation and assimilation with high res-

olution models. Berichte aus dem Institut für Meereskunde an der Universität Kiel Tech. Rep. 294, 334 pp.

Ellison, T. H., and J. S. Turner, 1959: Turbulent entrainment in stratified flows. *J. Fluid Mech.,* **6,** 423–448.

Flierl, G. R., M. E. Stern, and J. A. Whitehead, 1981: The physical significance of modons: Laboratory experiments and general integral constraints. *Dyn. Atmos. Oceans,* **7,** 233–263.

Gawarkiewicz, G., and D. C. Chapman, 1995: A numerical study of dense water formation and transport on a shallow, sloping continental shelf. *J. Geophys. Res.,* **100,** 4489–4507.

Gazdag, J., 1976: Time-differencing schemes and transform methods. *J. Comput. Phys.,* **20,** 196–207.

Griffiths, R. W., 1986: Gravity currents in rotating systems. *Annu. Rev. Fluid Mech.,* **18,** 59–89.

——, and E. J. Hopfinger, 1983: Gravity currents moving along a lateral boundary in a rotating fluid. *J. Fluid Mech.,* **134,** 357–399.

Hacker, J., P. F. Linden, and S. B. Dalziel, 1996: Mixing in lock-release gravity currents. *Dyn. Atmos. Oceans,* **24,** 183–195.

Hallworth, M. A., H. E. Huppert, J. C. Phillips, and S. J. Sparks, 1996: Entrainment into two-dimensional and axisymmetric turbulent gravity currents. *J. Fluid Mech.,* **308,** 289–311.

Huppert, H. E., 1982: The propagation of two-dimensional and axisymmetric viscous gravity currents over a rigid horizontal surface. *J. Fluid Mech.,* **121,** 43–58.

Jia, Y., 2000: On the formation of an Azores Current due to Mediterranean overflow in a modelling study of the North Atlantic. *J. Phys. Oceanogr.,* **30,** 2342–2358.

Jiang, L., and R. W. Garwood Jr., 1995: A numerical study of three-dimensional dense bottom plumes on a Southern Ocean continental slope. *J. Geophys. Res.,* **100,** 18 471–18 488.

——, and ——, 1996: Three-dimensional simulations of overflows on continental slopes. *J. Phys. Oceanogr.,* **26,** 1214–1233.

——, and ——, 1998: Effects of topographic steering and ambient stratification on overflows on continental slopes: A model study. *J. Geophys. Res.,* **103,** 5459–5476.

Jungclaus, J. H., and J. O. Backhaus, 1994: Application of a transient reduced gravity plume model to the Denmark Strait Overflow. *J. Geophys. Res.,* **99,** 12 375–12 396.

Kao, T. W., C. Park, and H.-P. Pao, 1978: Inflows, density currents, and fronts. *Phys. Fluids,* **21,** 1912–1923.

Keulegan, G. H., 1958: The motion of saline fronts in still water. U.S. Natl. Bur. Stand., Rep. 5831.

Killworth, P. D., 1977: Mixing on the Weddell Sea continental slope. *Deep-Sea Res.,* **24,** 427–448.

Ledwell, J. R., A. J. Watson, and C. S. Law, 1993: Evidence for slow mixing across the pycnocline from an open-ocean tracer-release experiment. *Nature,* **364,** 701–703.

Lesieur, M., 1997: *Turbulence in Fluids.* 3d ed. Kluwer, 515 pp.

Lozier, M. S., W. B. Owens, and R. G. Curry, 1995: The climatology of the North Atlantic. *Progress in Oceanography,* Vol. 36, 1–44.

Marmorino, G. O., 1987: Observations of small-scale mixing processes in the seasonal thermocline. Part II: Wave breaking. *J. Phys. Oceanogr.,* **17,** 1348–1355.

Meleshko, V. V., and G. J. F. Van Heijst, 1995: Interacting two-dimensional vortex structures: Point vortices, contour kinematics and stirring properties. *Chaos Applied to Fluid Mixing,* H. Aref and M. S. El Naschie, Eds., Pergamon, 233–266.

Middleton, G. V., 1966: Experiments on density and turbidity currents. *Can. J. Earth Sci.,* **3,** 523–546.

Monaghan, J. J., R. A. F. Cas, A. M. Kos, and M. Hallworth, 1999: Gravity currents descending a ramp in a stratified tank. *J. Fluid Mech.,* **379,** 39–70.

Morton, B. R., G. I. Taylor, and J. S. Turner, 1956: Turbulent gravitational convection from maintained and instantaneous sources. *Proc. Roy. Soc. London,* **A234,** 1–23.

Murray, S. P., and W. E. Johns, 1997: Direct observations of seasonal exchange through the Bab el Mandab Strait. *Geophys. Res. Lett.,* **24,** 2557–2560.

Nielsen, A. H., and J. J. Rasmussen, 1996: Formation and temporal evolution of the Lamb-dipole. *Phys. Fluids,* **9,** 982–991.

Özgökmen, T. M., and E. P. Chassignet, 1998: The emergence of inertial gyres in a two-layer quasigeostrophic model. *J. Phys. Oceanogr.,* **28,** 461–484.

——, and O. E. Esenkov, 1998: Asymmetric salt fingers induced by a nonlinear equation of state. *Phys. Fluids,* **10,** 1882–1890.

——, E. P. Chassignet, and A. M. Paiva, 1997: Impact of wind forcing, bottom topography, and inertia on midlatitude jet separation in a quasigeostrophic model. *J. Phys. Oceanogr.,* **27,** 2460–2476.

——, O. E. Esenkov, and D. B. Olson, 1998: A numerical study of layer formation due to fingers in double-diffusive convection in a vertically-bounded domain. *J. Mar. Res.,* **56,** 463–487.

——, E. P. Chassignet, and C. G. H. Rooth, 2001: On the connection between the Mediterranean outflow and the Azores Current. *J. Phys. Oceanogr.,* **31,** 461–480.

Price, J. F., and M. O. Baringer, 1994: Outflows and deep water production by marginal seas. *Progress in Oceanography,* Vol. 33, Pergamon, 161–200.

——, and J. Yang, 1998: Marginal sea overflows for climate simulations. *Ocean Modelling and Parameterization,* E. P. Chassignet and J. Verron, Eds., Kluwer Academic, 155–170.

——, and Coauthors, 1993: Mediterranean outflow mixing and dynamics. *Science,* **259,** 1277–1282.

Simpson, J. E., 1969: A comparison between laboratory and atmospheric density currents. *Quart. J. Roy. Meteor. Soc.,* **95,** 758–765.

——, 1982: Gravity currents in the laboratory, atmosphere, and the ocean. *Annu. Rev. Fluid Mech.,* **14,** 213–234.

——, 1987: *Gravity Currents in the Environment and the Laboratory.* John Wiley and Sons, 244 pp.

——, and R. E. Britter, 1979: The dynamics of the head of a gravity current advancing over a horizontal surface. *J. Fluid Mech.,* **94,** 477–495.

Smith, P. C., 1975: A streamtube model for bottom boundary currents in the ocean. *Deep-Sea Res.,* **22,** 853–873.

Smith, R. A., 1991: Maximization of vortex entropy as an organizing principle in intermittent, decaying, two-dimensional turbulence. *Phys. Rev.,* **A43,** 1126–1129.

Swarztrauber, P. N., 1977: The methods of cyclic reduction, Fourier analysis and FACR algorithm for discrete solution of the Poisson equation an a rectangle. *SIAM Rev.,* **19,** 490–501.

Turner, J. S., 1962: The starting plume in neutral surroundings. *J. Fluid Mech.,* **13,** 356–368.

——, 1986: Turbulent entrainment: The development of the entrainment assumption, and its applications to geophysical flows. *J. Fluid Mech.,* **173,** 431–471.

Willebrand, J., and Coauthors, 2001: Circulation characteristics in three eddy-permitting models of the North Atlantic. *Progress in Oceanography,* Vol. 48, Pergamon, 123–161.

Winton, M., R. Hallberg, and A. Gnanadesikan, 1998: Simulation of density-driven frictional downslope flow in *z*-coordinate ocean models. *J. Phys. Oceanogr.,* **28,** 2163–2174.

Wood, I. R., 1965: Studies of unsteady self preserving turbulent flows. University of New South Wales, Australian Water Resource Laboratory Rep. 81.